

Self-assembly of aramid amphiphiles into ultra-stable nanoribbons and aligned nanoribbon threads

Ty Christoff-Tempesta ¹, Yukio Cho¹, Dae-Yoon Kim¹, Michela Geri ¹, Guillaume Lamour ², Andrew J. Lew ³, Xiaobing Zuo ⁴, William R. Lindemann¹ and Julia H. Ortony ¹

Small-molecule self-assembly is an established route for producing high-surface-area nanostructures with readily customizable chemistries and precise molecular organization. However, these structures are fragile, exhibiting molecular exchange, migration and rearrangement—among other dynamic instabilities—and are prone to dissociation upon drying. Here we show a small-molecule platform, the aramid amphiphile, that overcomes these dynamic instabilities by incorporating a Kevlar-inspired domain into the molecular structure. Strong, anisotropic interactions between aramid amphiphiles suppress molecular exchange and elicit spontaneous self-assembly in water to form nanoribbons with lengths of up to 20 micrometres. Individual nanoribbons have a Young's modulus of 1.7 GPa and tensile strength of 1.9 GPa. We exploit this stability to extend small-molecule self-assembly to hierarchically ordered macroscopic materials outside of solvated environments. Through an aqueous shear alignment process, we organize aramid amphiphile nanoribbons into arbitrarily long, flexible threads that support 200 times their weight when dried. Tensile tests of the dry threads provide a benchmark for Young's moduli (between ~400 and 600 MPa) and extensibilities (between ~0.6 and 1.1%) that depend on the counterion chemistry. This bottom-up approach to macroscopic materials could benefit solid-state applications historically inaccessible by self-assembled nanomaterials.

pontaneous self-assembly of small amphiphilic molecules in water provides a powerful route to nanoscale structures with molecular-scale dimensions and pristine internal organization^{1,2}. High-aspect-ratio nanostructures afforded by molecular self-assembly may be entangled or aligned, while maintaining high surface areas and tunable surface chemistries3,4. However, these supramolecular structures are generally fragile due to their weak intermolecular interactions^{5,6} and pervasive dynamic instabilities that is, molecular exchange, migration, insertions, rearrangements and transpositions⁷⁻⁹. Further, internal transient water contributes to the vulnerability of amphiphilic nanostructures by facilitating enzymatic or hydrolytic degradation^{10,11}. Because of these limitations, small-molecule assemblies are generally developed for biomaterials applications, where fast dynamics and biodegradability are harnessed as key design features 12-14. These properties preclude their use in air, where they lack the structural stability imposed via the hydrophobic effect that is required to hold them together. Therefore, an amphiphile self-assembly platform that minimizes dynamics is an important target and could provide an approach to solid-state applications for which precise molecular organization, nanoscale structure, tunable surface chemistries and water processability are desirable¹⁵. Such solid-state applications could range from ion transporting to thermally conductive soft materials 16,17.

A reliable strategy for enhancing mechanical properties of molecular materials is to incorporate hydrogen bonding domains into the molecular design¹⁸. For example, the collective hydrogen bonding between aromatic amides (aramids) in Kevlar (poly(*p*-phenylene terephthalamide)) leads to its renowned strength and impact

resistance¹⁹. Similar aramid chemical motifs have been incorporated into the design of biomimetic peptide-based amphiphiles 20,21; however, in these cases, the impact of the aramid domains on the mechanical properties remains unknown. In contrast to small amphiphilic molecules, polymeric aramid nanofibres composed of poly(p-phenylene terephthalamide) have shown strong mechanical behaviour²², even upon drying, but neither control over nanofibre surface chemistry nor precise internal molecular organization is achievable. In a handful of cases, molecules containing aramid moieties have aggregated in a variety of solvents into short rod-like or hockey-puck micelles, with the longest dimension on the order of tens or hundreds of nanometres^{23–25}. Despite these contributions, rational design of amphiphiles to form mechanically robust high-aspect-ratio nanostructures, and the processing of these nanostructures into aligned solid-state one-dimensional materials, remains an important goal.

Here we show a molecular design motif that incorporates aramids as a structural domain within small-molecule amphiphiles. These molecules, aramid amphiphiles (AAs), spontaneously self-assemble upon addition of water to form nanoribbons. AA nanoribbons are designed to be intrinsically hydrolysis resistant, containing amides that are buried in the hydrophobic interior of the nanostructure, away from water¹⁰. AAs incorporate three attributes to suppress exchange dynamics and to enhance mechanical properties: (1) a high hydrogen bond density, with six hydrogen bonds per molecule; (2) in-register organization within each hydrogen bond network and the ability to form interplane π – π stacking²⁶; and (3) minimal steric packing strain and torsion to minimize hydrogen

¹Department of Materials Science and Engineering, Massachusetts Institute of Technology, Cambridge, MA, USA. ²LAMBE, Université Paris-Saclay, University of Evry, CNRS, Evry-Courcouronnes, France. ³Department of Chemistry, Massachusetts Institute of Technology, Cambridge, MA, USA. ⁴X-ray Science Division, Advanced Photon Source, Argonne National Laboratory, Argonne, IL, USA. ⁵Present address: Institute of Advanced Composite Materials, Korea Institute of Science and Technology, Bondong, Korea. [™]e-mail: ortony@mit.edu

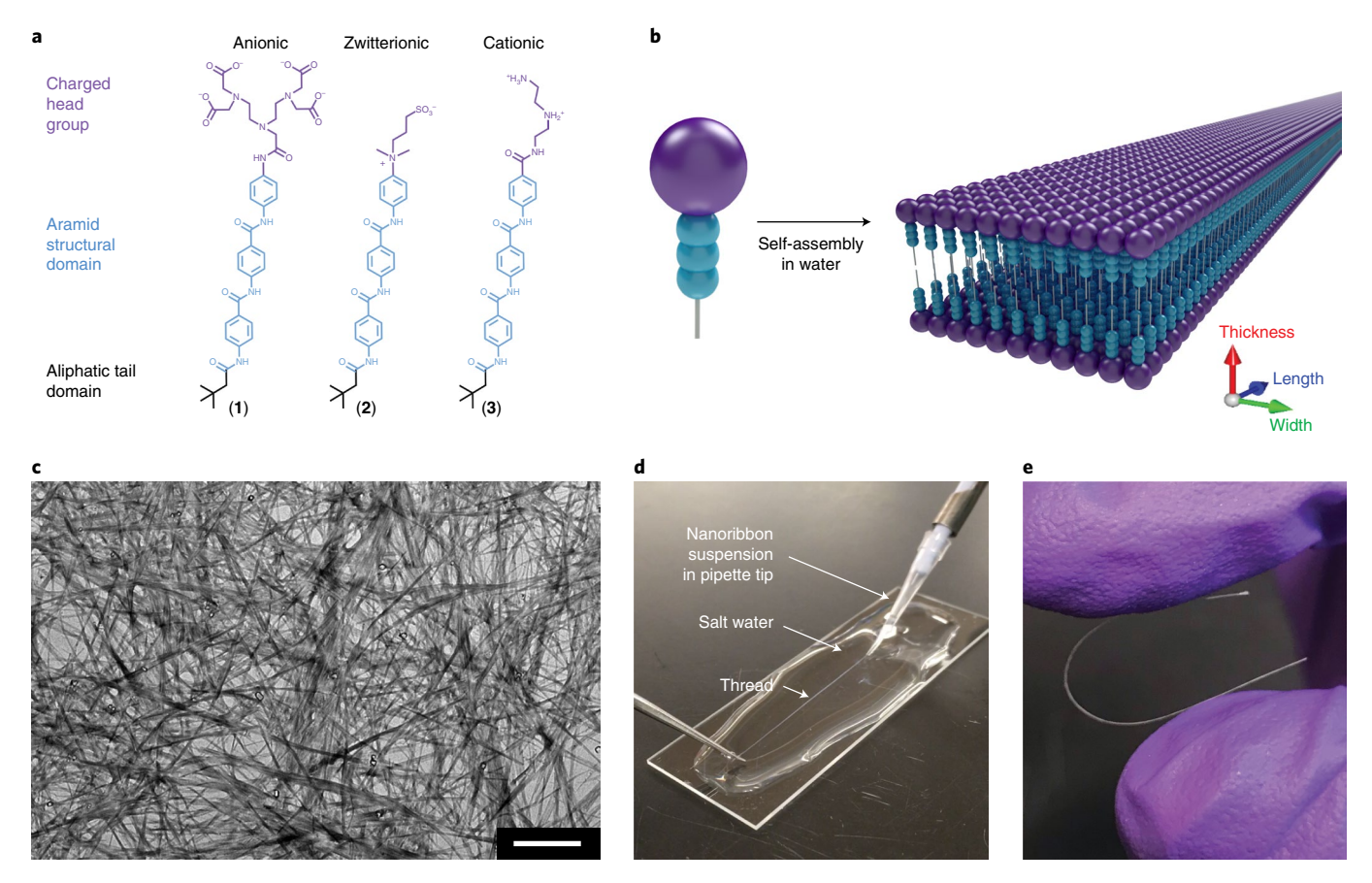


Fig. 1 [Kevlar-inspired AAs self-assemble into ultra-stable nanoribbons capable of hierarchical ordering to form dry macroscopic threads. **a**, AAs are composed of a charged head group and an aliphatic tail to induce amphiphilic self-assembly, and an aramid structural domain to yield collective intermolecular hydrogen bonding. AAs **1**, **2** and **3** have anionic, zwitterionic and cationic head groups, respectively. **b**, AAs are designed to spontaneously self-assemble in water into nanoribbons with suppressed exchange dynamics. **c**, Dried nanoribbons of **2** are observed in a representative TEM micrograph (scale bar, 1μm). **d**, A nanoribbon suspension (compound **3**) is pulled out of a pipette tip by tweezers into a sodium sulfate solution to form a one-dimensional gel. **e**, The gel is removed from water and dried to form a thread composed of aligned nanoribbons that can be bent and handled easily. Panel **b** adapted with permission from ref. ⁵⁸, Cell Press.

bond distances²⁷, achieved by incorporating unobtrusive amphiphile head and tail groups into the molecular design. As a result, these nanoribbons are candidates for alignment and removal from water while maintaining their structure to obtain macroscopic, air-stable threads.

Self-assembled nanoribbons with suppressed exchange dynamics

We synthesized AAs with three different head group chemistries to tune the surface charge of the nanoribbons (Fig. 1a): compound 1, an anionic pentetic acid amphiphile; compound 2, a zwitterionic ammonium sulfonate amphiphile; and compound 3, a cationic triazaheptane amphiphile (Supplementary Schemes 1–3 and Supplementary Figs. 1–16). The structural domains of compounds 1–3 contain three aramid repeat units, and the hydrophobic tails consist of branched, six-carbon neopentyl groups. These features are designed to elicit spontaneous self-assembly in water into nanostructures with strong intermolecular interactions (Fig. 1b).

We observe the assembly of 1, 2 and 3 in water into high-aspect-ratio nanoribbons by conventional transmission electron microscopy (TEM; Fig. 1c and Supplementary Fig. 21). The nanostructures' stability and high aspect ratios allow for shear alignment during gelation. This process leads to arbitrarily long threads (Fig. 1d) that remain intact when removed from water (Fig. 1e).

Small angle X-ray scattering (SAXS) profiles of compounds 1-3 in water fit most closely to a lamellar bilayer model (Fig. 2a and Supplementary Fig. 25)28,29. This fit gives a nanoribbon thickness of 3.9 nm for 1, 2 and 3, which is corroborated by atomic force microscopy (AFM) height profiles (Supplementary Fig. 28). The observed slope of -2 in the low-q regime of the SAXS profiles, where the scattering angle is small, further suggests one-dimensional nanostructures in solution³⁰. Cryogenic TEM (cryo-TEM) was used to image the nanoribbons in water at higher resolution for determining nanoribbon widths. Based on cryo-TEM, the widths of nanoribbons of 1, 2 and 3 are 5.5 nm, 5.1 nm and 5.8 nm, respectively (Fig. 2b and Supplementary Fig. 23). We find that the nanoribbon geometry is insensitive to temperature and concentration, with nanoribbons of 3 observed up to 80 °C and from 0.1 to 20 mg ml⁻¹, but are sensitive to pH (Supplementary Figs. 22 and 26). Interestingly, we observe that self-assembled AA nanoribbons elongate upon bath sonication (with powers of approximately 10 W l-1), reaching extraordinary lengths of up to 20 µm (refs. 31,32), corresponding to width-to-length aspect ratios of 4,000:1. Sonication has been previously shown to facilitate reorganization of hydrogen bonding in self-assembling systems³³. The observed high aspect ratios of AA nanoribbons confirm that highly anisotropic intermolecular interactions occur between the nanoribbon length and width axes (Supplementary Figs. 21 and 28).

ARTICLES

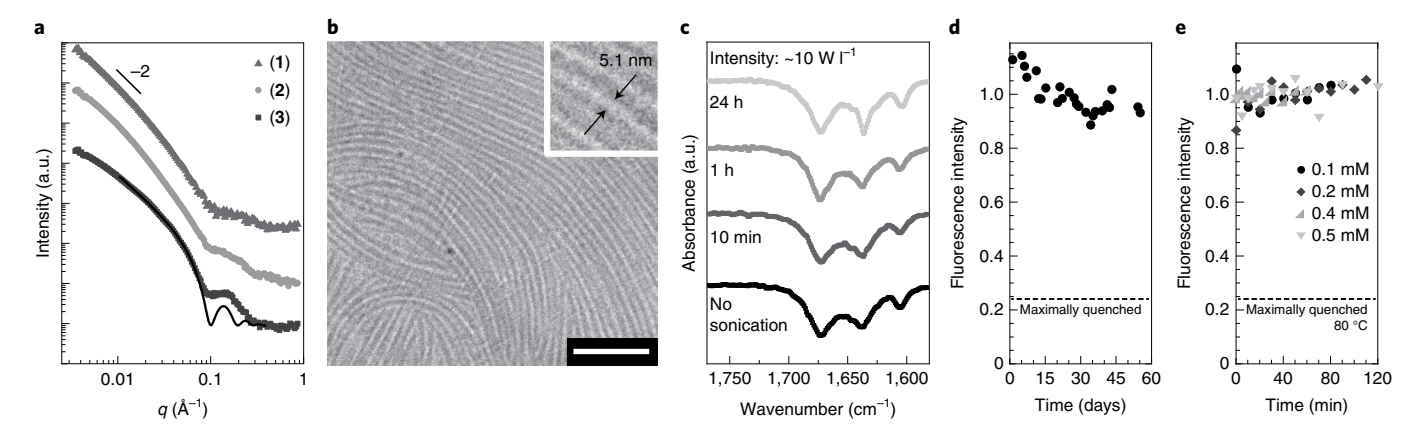


Fig. 2 | AA nanoribbons exhibit minimal molecular exchange. a, SAXS of compound **1, 2** and **3** nanoribbons in water shows a slope of -2 in the low-q regime, indicating high-aspect-ratio structures, and is best fit to a lamellar model (black line) giving a 3.9 nm nanoribbon thickness, consistent with nanoribbon geometries. **b**, Representative cryo-TEM image of nanoribbons of **2** in water reveals nanoribbon widths of \sim 5 nm (scale bar, 100 nm). **c**, ATR-FTIR of compound **3** nanoribbons shows the emergence of a sharp peak at 1,638 cm $^{-1}$ upon bath sonication, consistent with strengthening of the hydrogen bond network. **d**, Normalized fluorescence intensities of a 1:1 mixture of donor- and quencher-labelled nanoribbon suspensions are measured over 55 days. A nearly constant fluorescence intensity indicates minimal dark quenching and corresponds to minimal molecular exchange between nanoribbons over this time period. As a control, complete co-assembly of donor and quencher amphiphiles results in a 76% decrease in fluorescence intensity, illustrated by the horizontal dotted line (Supplementary Section 3f). **e**, Normalized fluorescence intensities of mixtures of donor- and quencher-labelled nanoribbon suspensions at 80 °C show that FRET dark quenching is not observed upon heating. This experiment was carried out with AA concentrations ranging from 0.1 to 0.5 mM, and no exchange is observed.

The nanoribbon geometry allows us to draw conclusions about the molecular packing. We observe, through AFM height profiles, a nanoribbon thickness approximately equal to two molecular lengths. Knowing that the hydrophilic head group must be exposed to water and the hydrophobic region (including the structural domain) must be shielded, we deduce that interdigitation between the molecules in the assembly must be limited to their short aliphatic tails. Concomitantly, we conclude that the molecules most likely adopt lamellar packing, which is corroborated by fits of SAXS profiles to a lamellar model (Fig. 2a and Supplementary Section 3c). This molecular arrangement deviates from the two-dimensional networks observed in solid-state crystals of oligomeric *p*-benzamide crystals^{34,35} since the driving force for amphiphilic self-assembly imposes orientational constraints that differ from those implicated in crystallization³⁶.

We performed attenuated total reflectance Fourier-transform infrared spectroscopy (ATR-FTIR) on solutions of compound 3 as a function of bath sonication time to observe the evolution of hydrogen bonding with nanoribbon formation in solution. Compound 3 nanoribbons were selected for this analysis because their solubility is high, and consequently they produce the strongest signal of compounds 1-3. However, molecular packing is likely dominated by the aramid structural domain, which is equivalent in all three AA compounds. Therefore, we expect the molecular packing of compound 3 to be representative of all the AA nanoribbons, 1-3, particularly because they all exhibit similar nanoribbon geometries. Shown in Fig. 2c, a peak at 1,638 cm⁻¹, corresponding to a carbonyl (C=O) amide I stretch and characteristic of β-sheet hydrogen bonding, becomes more pronounced as sonication time increases. The sharpening of this peak indicates that uniformity of intermolecular hydrogen bonding distances increases upon sonication, likely because sonication provides the necessary energy to overcome kinetic traps. As a control, addition of a denaturant, dimethylsulfoxide (DMSO), to the nanoribbon suspension results in a suppression of the amide I peak, consistent with disruption of the hydrogen bonding network (Supplementary Fig. 20). The peaks at 1,672 cm⁻¹ and 1,600 cm⁻¹ are assigned to carbonyl stretching of the amide

bond connecting the head group to the aramid structural domain and carbon–carbon stretching in the aromatic units, respectively, and their positions and intensities are therefore less sensitive to molecular packing (Supplementary Fig. 19)^{37,38}.

Collective hydrogen bonding within AA nanoribbons is expected to lead to strong internal cohesion and therefore slow molecular exchange dynamics⁶. We probed the rate at which individual AA molecules exchange between adjacent nanoribbons by Förster resonant energy transfer (FRET) dark quenching (Supplementary Section 3f)39. We mixed separate nanoribbon suspensions containing either fluorophore- or quencher-tagged amphiphiles and observed minimal molecular exchange between adjacent nanoribbons over 55 days (Fig. 2d). Further, no changes in peak fluorescence intensity were observed when mixtures of fluorophore- and quencher-labelled nanoribbons were heated to 80 °C over a range of concentrations (Fig. 2e). These results highlight the stability that aramid hydrogen bonding imparts on amphiphilic nanoribbon assemblies, representing a substantial departure from the typical exchange rates of 1-2h reported in phospholipid membranes and supramolecular peptide assemblies^{8,9}. The slow exchange dynamics of AA nanoribbons allow us to perform single-nanoribbon mechanical characterization experiments.

Mechanical properties of individual nanoribbons

Direct mechanical characterization of solid-state nanofibres has previously been demonstrated to yield stress–strain profiles via AFM force measurements 40,41. However, this method requires that the widths of the fibres are large relative to the radius of curvature of the AFM tip. In the case of small nanostructures whose widths are less than 10 nm, as observed in AA nanoribbons, direct mechanical measurements pose substantial experimental challenges. To circumvent the lower bound size limitation, indirect methods of nanofibre mechanical characterization have been developed 42–44. These methods are based on AFM imaging of nanofilaments or nanofilament fragments followed by statistical analyses to determine Young's moduli or tensile strengths. Such studies have uncovered mechanical properties of a range of nanofilaments with diameters on the

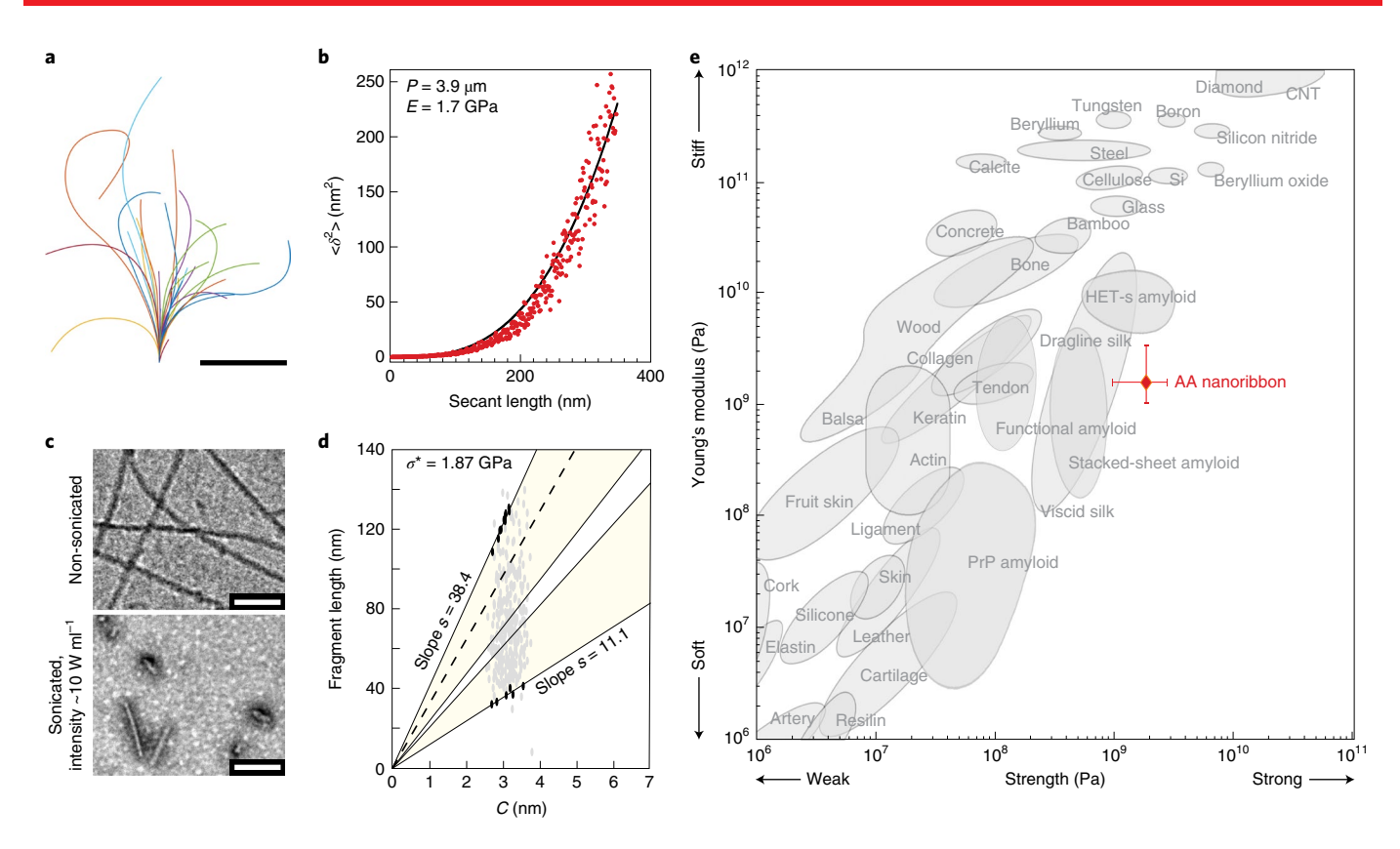


Fig. 3 | AA nanoribbons have a Young's modulus of E=1.7 GPa and a tensile strength of $\sigma^*=1.9$ GPa. **a**, Contours acquired by tracing the AFM profiles of 29 AA nanoribbons are used for statistical topographical analysis (scale bar, 1 μm). **b**, Midpoint deviations δ from contour traces are used to calculate a persistence length, $P=3.9\pm0.7$ μm and Young's modulus, $E=1.7\pm0.7$ GPa, from least-squares fitting of a worm-like chain model for semi-flexible polymers to the data. $<\delta^2>$ denotes the mean square of δ . **c**, Sonication-induced scission of nanoribbons, carried out with approximately 10 W ml⁻¹ horn sonication, is illustrated by TEM (scale bars, 100 nm). **d**, The threshold length $L_{\rm lim}$ below which a fibril will not break under sonication is determined from plotting sonicated fragment lengths against cross-sectional size, C. The yellow areas illustrate the broadened boundaries of the terminal range defined by ($L_{\rm lim}/2$, and the dashed line represents the average $L_{\rm lim}^{48}$. The tensile strength of AA nanoribbons is calculated to be $\sigma^*=1.87\pm1.00$ GPa. **e**, AA nanoribbon mechanical properties, shown on an Ashby plot, place it among the strongest and stiffest biological materials⁴⁸. Young's modulus and tensile strength values are reported as mean \pm standard deviation. CNT, carbon nanotube. Panel **e** adapted with permission from ref. ⁴⁸, Cell Press.

order of $10\,\mathrm{nm}$ including silver nanowires, carbon nanotubes and amyloid fibrils 42,44,45.

We characterized the Young's modulus of AA nanoribbons using statistical topographical analysis of AFM images. The Young's modulus of compound 3 nanoribbons was measured due to that compound's high solubility and for consistency among characterization techniques. Mechanical properties arise from the region with the strongest intermolecular interactions—the aramid structural domain—so we expect nanoribbons of 1 and 2 to exhibit similar Young's moduli and tensile strengths as compound 3. The shape fluctuations of compound 3 nanoribbons (number of nanoribbons n=29) in water equilibrated on a glass surface were used to determine their bending rigidity (Fig. 2d)^{42,43}. Parametric splines to the contours of each nanoribbon were traced (Fig. 3a) and fit to determine a persistence length, $P=3.9\pm0.7\,\mu\text{m}$, from which the Young's modulus was calculated to be $E=1.7\pm0.7\,\text{GPa}$ (Fig. 3b and Supplementary Section 3g).

The ultimate tensile strength (σ^*) of AA nanoribbons was determined by AFM statistical analysis after horn-sonication-induced scission, which produces nanostructure fragments in water below a threshold length, $L_{\rm lim}$ (refs. ^{44,46}). For clarity, horn sonication delivers 100 to 1,000 times greater sonication power intensity to the sample volume compared to bath sonication ⁴⁷, which was previously shown to reinforce the nanoribbon hydrogen bonding network by ATR-FTIR. From visualizing 400 horn sonicated fragments by TEM (Fig. 3c), $L_{\rm lim}$ for the nanoribbons was evaluated from their fragment

length distribution as $98\pm26\,\mathrm{nm}$, which corresponds to a tensile strength of $\sigma^*=1.87\pm1.00\,\mathrm{GPa}$ (Fig. 3d and Supplementary Section 3h). These mechanical properties place AA nanoribbons in a region of the Ashby plot viable for solid-state applications (Fig. 3e)⁴⁸.

Materials constructed of small-molecule amphiphile nanoribbons offer high surface areas, on the order of hundreds of metres squared per gram, dictated by the size of the constituent molecules. The tunable surface chemistries of such structures further allow for targeted interactions, and the capacity for co-assembly of different amphiphiles could allow such materials to perform multiple functions on the same surface^{49,50}. However, small-molecule nanostructures are often limited to solvated environments due to their fast dynamics and reliance on the hydrophobic effect to hold their structures together. We explored the potential of aligning AA nanoribbons into solid-state thread-like materials, a possibility enabled by their suppressed exchange dynamics and robust mechanical properties.

Alignment of nanoribbons into solid-state threads

A simple strategy for aligning self-assembled nanofibres into one-dimensional gels in water has been previously demonstrated³. In this approach, peptide amphiphiles were thermally annealed to form liquid crystalline bundles, which were shear aligned in divalent counterion solution to produce macroscopic one-dimensional gels³. These gels have been used for applications including cell scaffolding and protein delivery^{3,51}. We harnessed this processing

ARTICLES

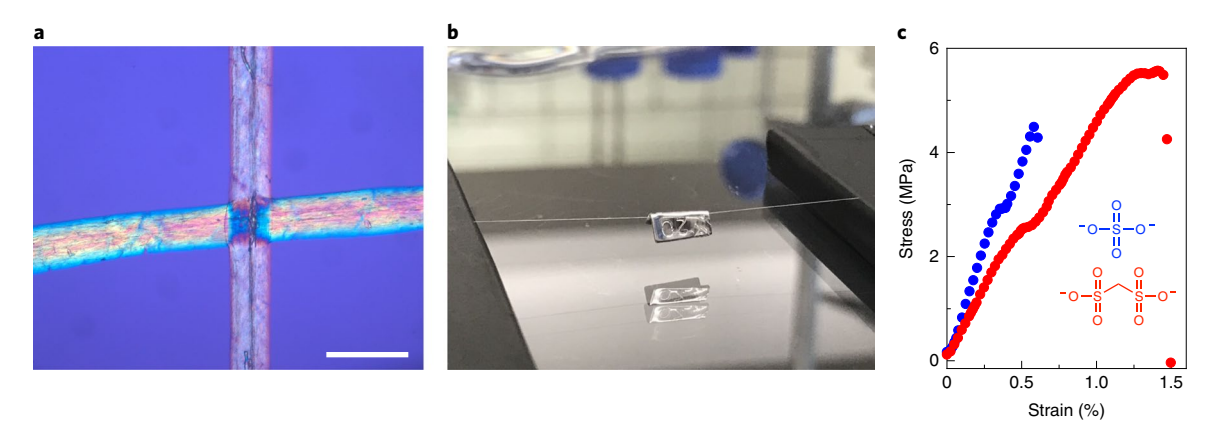


Fig. 4 | AA nanoribbons are aligned by shear forces and dried to form flexible threads. a, A polarized light micrograph shows the intersection of two nanoribbon threads. The birefringence observed under cross-polarizers indicates the nanoribbons are aligned within the threads (scale bar, $100 \, \mu m$). **b**, A 5 cm nanoribbon thread whose mass totals 0.1 mg is suspended over a trough and supports a 20 mg weight. **c**, Representative tensile tests of AA threads formed with sulfate (blue) and methanedisulfonate (red) counterions are shown. Tensile tests of twelve samples reveal Young's moduli of $637 \pm 114 \, MPa$ and $385 \pm 77 \, MPa$, respectively, and extensibility values of $0.6 \pm 0.2\%$ and $1.1 \pm 0.2\%$, respectively. Data are reported as mean \pm standard deviation.

strategy by annealing cationic nanoribbons (compound 3) in water and pulling the suspension through a salt solution (Na_2SO_4) on a glass slide (Fig. 1d). This process leads to the formation of a one-dimensional gel that exhibits birefringence under polarized light (Fig. 4a), indicating that the nanoribbons are aligned within the gel. We demonstrate the unique ability of the nanoribbon gel to withstand drying in air, forming a stable solid thread that can be handled and bent without breaking (Fig. 1e), and can support over 200 times its weight (Fig. 4b). Scanning electron microscopy (SEM) imaging of the AA threads in vacuum reveal thread diameters near 20 μ m and striations consistent with the presence of nanoribbon bundles (Supplementary Fig. 29).

The formation of solid-state nanoribbon threads requires that individual nanoribbons exhibit considerable structural integrity, which in the case of AAs is imparted by their aramid domain. However, neither the Young's modulus nor tensile strength of nanoribbons is expected to govern the threads' bulk mechanical properties. Rather, electrostatics dominate inter-ribbon interactions, an effect that has been previously demonstrated at highly charged nanoscale surfaces⁵². We hypothesize that adjusting the nanoribbon surface chemistry and counterion pair provides a route to adjusting the elastic modulus and extensibility of the thread. Consistent with this hypothesis, we find that gelation is possible only when the counterion valency is greater than one.

We performed tensile tests to determine the effect of counterion charge density on the threads' elastic moduli and extensibilities (Fig. 4c), providing a benchmark for future studies. Threads formed with two divalent anions—one with a high charge density (sulfate) and one with a lower charge density (methanedisulfonate)—were measured. Threads with sulfate and methanedisulfonate counterions produced Young's moduli of 637 ± 114 MPa and 385 ± 77 MPa, respectively (Supplementary Fig. 35). As one point of comparison, the observed modulus values fall on the same order of magnitude as those of polyethylenes⁵³. Further, we find that threads with the methanedisulfonate anion (elongation at break, $\varepsilon_{\text{break}} = 1.1 \pm 0.2\%$) are nearly twice as extensible as threads formed with the sulfate anion ($\varepsilon_{\text{break}} = 0.6 \pm 0.2\%$; Supplementary Fig. 36). We attribute the enhanced elastic modulus and decrease in extensibility of threads with sulfate counterions, compared to those with methanedisulfonate counterions, to the enhanced electrostatic interaction strengths between nanoribbons with counterions of greater charge densities⁵⁴. These experiments reveal that nanoribbon surface and counterion chemistry are viable parameters to vary for controlling bulk mechanical properties.

Hierarchical order within dry nanoribbon threads

We used X-ray scattering to study the structure within the nanoribbon thread and to confirm that nanoribbons remain intact after alignment and drying (Fig. 5a). Wide-angle X-ray scattering (WAXS) of the dried thread in vacuum shows anisotropic peaks indicating nanoribbon alignment, with the strongest WAXS peak occurring at a *d*-spacing of 5.05 Å (Fig. 5b). WAXS patterns of vertically oriented nanoribboon threads were collected and integrated to yield meridional and equitorial peaks. From these peaks, a simulated unit cell shows molecular packing resembling poly(p-benzamide) (Fig. 5c and Supplementary Section 3c)55. This structure implies that even upon drying in vacuum, where the hydrophobic effect is absent, intermolecular aramid hydrogen bonding is dominant along the nanoribbon long axis with H-O hydrogen bond distances of 2.08 Å. Further, we infer that $\pi - \pi$ stacking at an interplane distance of 3.61 Å laterally holds together hydrogen bonded sheets across the nanoribbon width (Fig. 5d).

The anisotropy observed by X-ray scattering confirms the geometric configuration of the AA structures as nanoribbons within the solid-state thread. The uniform intermolecular distances of 5.05 Å observed along the length of the nanoribbon indicate that an extended hydrogen bonding network is likely unencumbered by torsion or strain. This observation is consistent with the absence of helical nanoribbons, as well as the extraordinary nanoribbon lengths. The attractive forces along the nanoribbon width are substantially weaker, dominated by π - π stacking at an off-ribbon axis angle of 64°. This π - π stacking enables lateral growth of the ribbons, but leads to dimensions of only approximately 5 nm in width. Differences in intermolecular interaction strength along the nanoribbon long axes versus across the widths have previously been shown to lead to high-aspect-ratio nanoribbons as opposed to lamellar sheets⁵⁶.

While X-ray scattering supports the presence of nanoribbon geometries with rectangular cross-sections, this technique is largely insensitive to disordered and highly hydrated domains such as the head group domains of AA nanoribbons. Therefore, the scattering information used to designate the nanoribbons as planar with rectangular cross-sections arises primarily from the structured aramid domains. In reality, the head group domains of the nanoribbon are likely to survey the space surrounding the energetically disfavorable hydrophobic edge, shielding this region from solvent. The ability of the head groups to shield the nanoribbon edge is determined by head group size, hydration and intermolecular electrostatic repulsion. Consequences of this effect include that the nanorib-

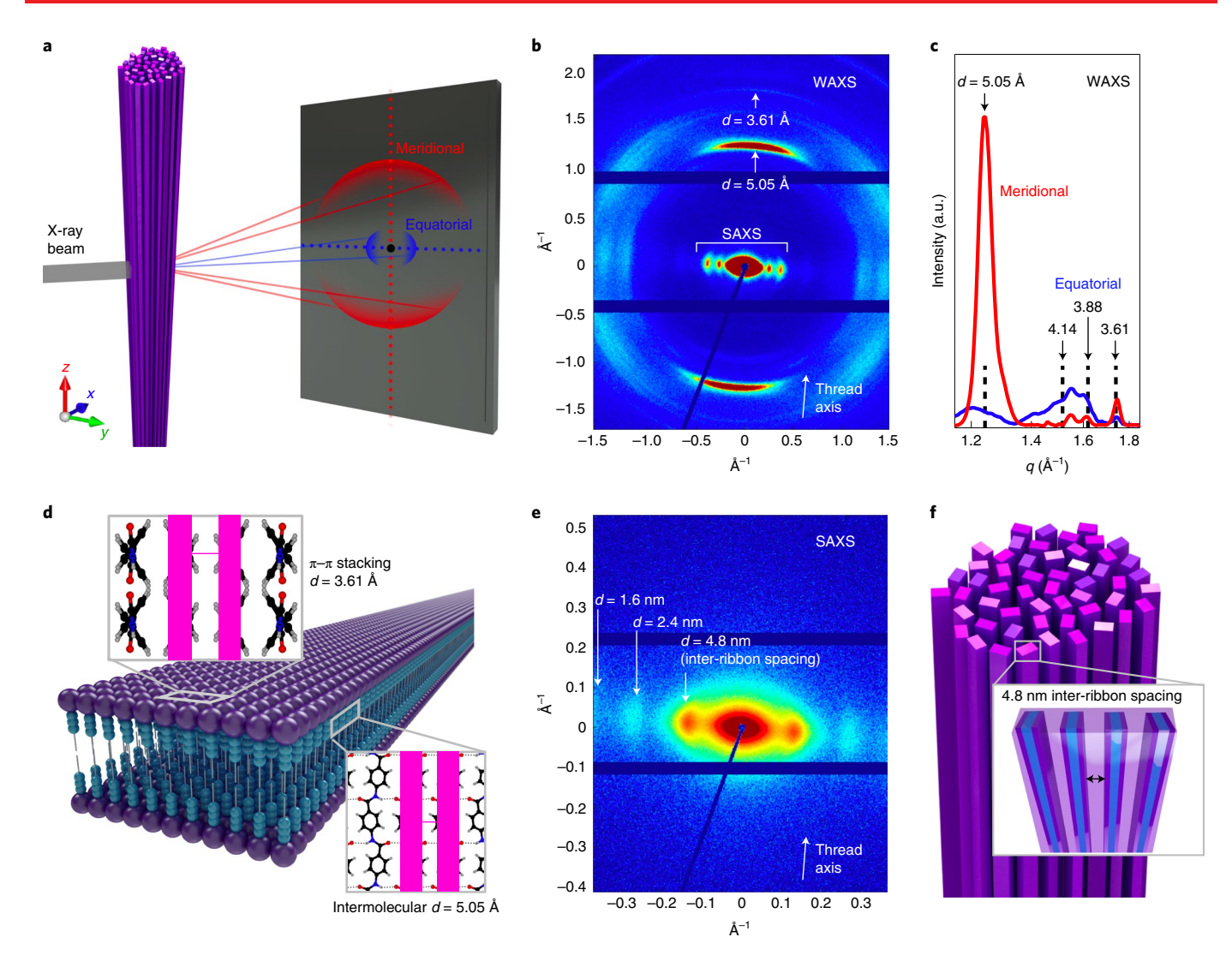


Fig. 5 | X-ray scattering of solid-state nanoribbon threads demonstrates organized molecular packing, extended hydrogen bonding networks and long-range hierarchical order. a, Meridional and equatorial scattering directions are depicted in X-ray scattering measurements of solid, aligned AA nanoribbon threads. **b**, A WAXS pattern of an AA nanoribbon thread indicates that precise molecular organization is maintained in the solid state, with anisotropy consistent with nanoribbon alignment. **c**, A one-dimensional scattering profile is obtained by integrating meridional and equatorial axes of **b**. Black dotted lines are simulated peak positions of a unit cell with a = 7.22 Å, b = 5.05 Å and c = 11.10 Å, and space group $26:Pmc2_1$ based on poly(p-benzamide). Colours towards the red end of the visible spectrum correspond to signal of higher intensity. **d**, Molecular packing in AA nanoribbons is illustrated as informed by the simulated unit cell in **c**; 5.05 Å intermolecular distances are observed, corresponding to hydrogen bonds of 2.08 Å (dotted lines in bottom inset) that form a network down the long axis of the nanoribbon; 3.61 Å intermolecular π - π stacking lies at a 64° tilt with respect to the hydrogen bonding plane. Based on these distances, the surface area of AA nanoribbons within the thread is $200 \, \text{m}^2 \, \text{g}^{-1}$. **e**, SAXS of an AA nanoribbon thread shows anisotropic lamellar peaks corresponding to a $4.8 \, \text{nm}$ lamellar spacings informed by **e**. Panel **d** adapted with permission from ref. 58 , Cell Press.

bon cross-sections are not perfectly rectangular but are rather distorted around the hydrophobic edge. Further, the nanoribbon width should be variable and sensitive to head group chemistry, while the length and thickness are not. To test this hypothesis, we synthesized AAs with neutral oligoethylene glycol head groups (OEG-AAs; Supplementary Section 1f). OEG-AA is expected to exhibit minimal head group repulsion, leading to wider nanoribbons. Upon self-assembly in water, OEG-AA nanoribbon thicknesses and lengths are found to be comparable to nanoribbons of 1, 2 and 3. Consistent with our hypothesis, we find their widths to be greater than those of 1, 2 and 3 nanoribbons, measured by cryo-TEM to be 7.0 nm (Supplementary Fig. 24).

Using the dimensions and spacings of compound 3 nanoribbons determined by X-ray scattering, we calculate a surface area within

the dried thread of 200 m² g⁻¹. At longer length scales, SAXS peaks in the equatorial direction result from AA nanoribbons aligned along the thread axis (Fig. 5e), with 4.8 nm spacings between nanoribbons (Fig. 5f). This spacing implies that most of the nanoribbon surfaces are accessible, even in the solid state. AA threads offer precise internal molecular structure, uniform inter-ribbon spacings and tunable nanoribbon surface chemistries in a macroscopic one-dimensional material from small-molecule amphiphilic self-assembly 16,17,57 .

Conclusions

We have presented a molecular self-assembly platform, the aramid amphiphile. Six hydrogen bonds fix each AA molecule within an extended network, which, when combined with lateral π - π stacking, gives rise to nanoribbons with 4 nm thicknesses, 5–6 nm widths

NATURE NANOTECHNOLOGY ARTICLES

and lengths of up to $20\,\mu m$. These nanoribbons exhibit slow molecular exchange dynamics, and tensile strengths and Young's moduli on the order of gigapascals. We apply a shear alignment technique to form macroscopic threads composed of aligned nanoribbon bundles with uniform 4.8 nm inter-ribbon spacings and surface areas of $200\,m^2\,g^{-1}$. We propose the choice of nanoribbon head group and counterion chemistry as features that may be modified to optimize bulk mechanical properties. Further, we demonstrate that these nanoribbon threads are flexible, can be handled and can support 200 times their weight, making them suitable for solid-state applications. The AA platform overcomes dynamic instabilities common in supramolecular small-molecule assemblies and provides a route to nanostructured, solid-state molecular materials.

Online content

Any methods, additional references, Nature Research reporting summaries, source data, extended data, supplementary information, acknowledgements, peer review information; details of author contributions and competing interests; and statements of data and code availability are available at https://doi.org/10.1038/s41565-020-00840-w.

Received: 14 May 2020; Accepted: 10 December 2020; Published online: 18 January 2021

References

- Whitesides, G. M., Mathias, J. P. & Seto, C. T. Molecular self-assembly and nanochemistry: a chemical strategy for the synthesis of nanostructures. *Science* 254, 1312–1319 (1991).
- Aida, T., Meijer, E. & Stupp, S. I. Functional supramolecular polymers. Science 335, 813–817 (2012).
- Zhang, S. et al. A self-assembly pathway to aligned monodomain gels. Nat. Mater. 9, 594–601 (2010).
- Koutsopoulos, S., Unsworth, L. D., Nagai, Y. & Zhang, S. Controlled release of functional proteins through designer self-assembling peptide nanofiber hydrogel scaffold. *Proc. Natl Acad. Sci. USA* 106, 4623–4628 (2009).
- Tantakitti, F. et al. Energy landscapes and functions of supramolecular systems. Nat. Mater. 15, 469–476 (2016).
- Ortony, J. H. et al. Internal dynamics of a supramolecular nanofibre. *Nat. Mater.* 13, 812–816 (2014).
- Schief, W., Touryan, L., Hall, S. & Vogel, V. Nanoscale topographic instabilities of a phospholipid monolayer. J. Phys. Chem. B 104, 7388–7393 (2000).
- da Silva, R. M. et al. Super-resolution microscopy reveals structural diversity in molecular exchange among peptide amphiphile nanofibres. *Nat. Commun.* 7, 11561 (2016).
- Wimley, W. C. & Thompson, T. E. Transbilayer and interbilayer phospholipid exchange in dimyristoylphosphatidylcholine/ dimyristoylphosphatidylethanolamine large unilamellar vesicles. *Biochemistry* 30, 1702–1709 (1991).
- Ortony, J. H. et al. Water dynamics from the surface to the interior of a supramolecular nanostructure. J. Am. Chem. Soc. 139, 8915–8921 (2017).
- Yuan, D., Shi, J., Du, X., Zhou, N. & Xu, B. Supramolecular glycosylation accelerates proteolytic degradation of peptide nanofibrils. *J. Am. Chem. Soc.* 137, 10092–10095 (2015).
- Toledano, S., Williams, R. J., Jayawarna, V. & Ulijn, R. V. Enzyme-triggered self-assembly of peptide hydrogels via reversed hydrolysis. *J. Am. Chem. Soc.* 128, 1070–1071 (2006).
- Freeman, R. et al. Reversible self-assembly of superstructured networks. Science 362, 808–813 (2018).
- Williams, R. J. et al. Enzyme-assisted self-assembly under thermodynamic control. Nat. Nanotechnol. 4, 19–24 (2009).
- Hashim, P., Bergueiro, J., Meijer, E. & Aida, T. Supramolecular polymerization: a conceptual expansion for innovative materials. *Prog. Polym.* Sci. 105, 101250 (2020).
- Xu, Y. et al. Nanostructured polymer films with metal-like thermal conductivity. Nat. Commun. 10, 1771 (2019).
- Tuller, H. L. Ionic conduction in nanocrystalline materials. Solid State Ion. 131, 143–157 (2000).
- Sherrington, D. C. & Taskinen, K. A. Self-assembly in synthetic macromolecular systems via multiple hydrogen bonding interactions. Chem. Soc. Rev. 30, 83–93 (2001).
- Dobb, M., Johnson, D. & Saville, B. Supramolecular structure of a high-modulus polyaromatic fiber (Kevlar 49). *J. Polym. Sci. Polym. Phys. Ed.* 15, 2201–2211 (1977).

 Seyler, H., Storz, C., Abbel, R. & Kilbinger, A. F. A facile synthesis of aramide-peptide amphiphiles. Soft Matter 5, 2543–2545 (2009).

- Claussen, R. C., Rabatic, B. M. & Stupp, S. I. Aqueous self-assembly of unsymmetric peptide bolaamphiphiles into nanofibers with hydrophilic cores and surfaces. J. Am. Chem. Soc. 125, 12680–12681 (2003).
- Yang, M. et al. Dispersions of aramid nanofibers: a new nanoscale building block. ACS Nano 5, 6945–6954 (2011).
- Schleuss, T. W. et al. Hockey-puck micelles from oligo(p-benzamide)b-PEG rod-coil block copolymers. Angew. Chem. Int. Ed. 45, 2969–2975 (2006).
- Bohle, A. et al. Hydrogen-bonded aggregates of oligoaramide—poly(ethylene glycol) block copolymers. *Macromolecules* 43, 4978–4985 (2010).
- Abbel, R., Schleuss, T. W., Frey, H. & Kilbinger, A. F. M. Rod-length dependent aggregation in a series of oligo(*p*-benzamide)-*block*poly(ethylene glycol) rod-coil copolymers. *Macromol. Chem. Phys.* 206, 2067–2074 (2005).
- Johansson, A., Kollman, P., Rothenberg, S. & McKelvey, J. Hydrogen bonding ability of the amide group. J. Am. Chem. Soc. 96, 3794–3800 (1974).
- Dixon, D. A., Dobbs, K. D. & Valentini, J. J. Amide-water and amide-amide hydrogen bond strengths. J. Phys. Chem. 98, 13435–13439 (1994).
- Kline, S. R. Reduction and analysis of SANS and USANS data using IGOR Pro. J. Appl. Crystallogr. 39, 895–900 (2006).
- Nallet, F., Laversanne, R. & Roux, D. Modelling X-ray or neutron scattering spectra of lyotropic lamellar phases: interplay between form and structure factors. J. Phys. II 3, 487–502 (1993).
- Mertens, H. D. & Svergun, D. I. Structural characterization of proteins and complexes using small-angle X-ray solution scattering. *J. Struct. Biol.* 172, 128–141 (2010).
- Yokoi, H., Kinoshita, T. & Zhang, S. Dynamic reassembly of peptide RADA16 nanofiber scaffold. *Proc. Natl Acad. Sci. USA* 102, 8414–8419 (2005).
- Hartgerink, J. D., Beniash, E. & Stupp, S. I. Self-assembly and mineralization of peptide-amphiphile nanofibers. Science 294, 1684–1688 (2001).
- Cravotto, G. & Cintas, P. Molecular self-assembly and patterning induced by sound waves. The case of gelation. *Chem. Soc. Rev.* 38, 2684–2697 (2009).
- 34. Gorelik, T. E., van de Streek, J., Kilbinger, A. F., Brunklaus, G. & Kolb, U. Ab-initio crystal structure analysis and refinement approaches of oligo p-benzamides based on electron diffraction data. Acta Crystallogr. B Struct. Sci. 68, 171–181 (2012).
- Gorelik, T. et al. H-bonding schemes of di- and tri-p-benzamides assessed by a combination of electron diffraction, X-ray powder diffraction and solid-state NMR. CrystEngComm 12, 1824–1832 (2010).
- Wang, J., Liu, K., Xing, R. & Yan, X. Peptide self-assembly: thermodynamics and kinetics. Chem. Soc. Rev. 45, 5589–5604 (2016).
- Barth, A. Infrared spectroscopy of proteins. Biochim. Biophys. Acta Bioenerg. 1767, 1073–1101 (2007).
- Zandomeneghi, G., Krebs, M. R., McCammon, M. G. & Fändrich, M. FTIR reveals structural differences between native β-sheet proteins and amyloid fibrils. Protein Sci. 13, 3314–3321 (2004).
- Matayoshi, E. D., Wang, G. T., Krafft, G. A. & Erickson, J. Novel fluorogenic substrates for assaying retroviral proteases by resonance energy transfer. *Science* 247, 954–958 (1990).
- Wu, B., Heidelberg, A. & Boland, J. J. Mechanical properties of ultrahigh-strength gold nanowires. *Nat. Mater.* 4, 525–529 (2005).
- Smith, J. F., Knowles, T. P., Dobson, C. M., MacPhee, C. E. & Welland, M. E. Characterization of the nanoscale properties of individual amyloid fibrils. *Proc. Natl Acad. Sci. USA* 103, 15806–15811 (2006).
- Knowles, T. P. et al. Role of intermolecular forces in defining material properties of protein nanofibrils. Science 318, 1900–1903 (2007).
- Lamour, G., Kirkegaard, J. B., Li, H., Knowles, T. P. & Gsponer, J. Easyworm: an open-source software tool to determine the mechanical properties of worm-like chains. Source Code Biol. Med. 9, 16 (2014).
- Huang, Y. Y., Knowles, T. P. & Terentjev, E. M. Strength of nanotubes, filaments, and nanowires from sonication-induced scission. *Adv. Mater.* 21, 3945–3948 (2009).
- Nassar, R., Wong, E., Gsponer, J. & Lamour, G. Inverse correlation between amyloid stiffness and size. J. Am. Chem. Soc. 141, 58–61 (2019).
- Peng, Z. et al. High tensile strength of engineered β-solenoid fibrils via sonication and pulling. *Biophys. J.* 113, 1945–1955 (2017).
- Santos, H. M., Lodeiro, C. & Capelo-Martínez, J.-L. in *Ultrasound in Chemistry: Analytical Applications* 1–16 (Wiley Online Library, 2009).
- Lamour, G. et al. Mapping the broad structural and mechanical properties of amyloid fibrils. *Biophys. J.* 112, 584–594 (2017).
- Zhao, X. et al. Molecular self-assembly and applications of designer peptide amphiphiles. Chem. Soc. Rev. 39, 3480–3498 (2010).
- Niece, K. L., Hartgerink, J. D., Donners, J. J. & Stupp, S. I. Self-assembly combining two bioactive peptide-amphiphile molecules into nanofibers by electrostatic attraction. J. Am. Chem. Soc. 125, 7146–7147 (2003).

- Angeloni, N. L. et al. Regeneration of the cavernous nerve by Sonic hedgehog using aligned peptide amphiphile nanofibers. *Biomaterials* 32, 1091–1101 (2011).
- Fink, L., Steiner, A., Szekely, O., Szekely, P. & Raviv, U. Structure and interactions between charged lipid membranes in the presence of multivalent ions. *Langmuir* 35, 9694–9703 (2019).
- Knowles, T. P. & Buehler, M. J. Nanomechanics of functional and pathological amyloid materials. *Nat. Nanotechnol.* 6, 469–479 (2011).
- Bradbury, R. & Nagao, M. Effect of charge on the mechanical properties of surfactant bilayers. Soft Matter 12, 9383–9390 (2016).
- Takahashi, Y., Ozaki, Y., Takase, M. & Krigbaum, W. Crystal structure of poly(p-benzamide). J. Polym. Sci. B Polym. Phys. 31, 1135–1143 (1993).
- Paramonov, S. E., Jun, H.-W. & Hartgerink, J. D. Self-assembly of peptide amphiphile nanofibers: the roles of hydrogen bonding and amphiphilic packing. J. Am. Chem. Soc. 128, 7291–7298 (2006).
- 57. Russell, P. Photonic crystal fibers. Science 299, 358-362 (2003).
- Lindemann, W. R., Christoff-Tempesta, T. & Ortony, J. H. A global minimization toolkit for batch-fitting and χ² cluster analysis of CW-EPR spectra. *Biophys. J.* 119, 1937–1945 (2020).

Publisher's note Springer Nature remains neutral with regard to jurisdictional claims in published maps and institutional affiliations.

© The Author(s), under exclusive licence to Springer Nature Limited 2021

NATURE NANOTECHNOLOGY ARTICLES

Methods

Synthesis of AAs. The syntheses used in this study involve (1) carbodiimide-mediated coupling reactions to form amide linkages, (2) conventional deprotection reactions of *tert*-butyloxycarbonyl (Boc) and (3) hydrolysis of ester functionalities to produce carboxylic acid moieties. As the only exception, the zwitterionic head group of **2** is obtained by quaternization of a tertiary amine with a propanesultone. Both ¹H and ¹³C nuclear magnetic resonance (NMR; Supplementary Section 2a; Bruker Avance III DPX 400) and mass spectrometry (MS; Supplementary Section 2b; Bruker Omniflex) were used to confirm the chemical composition of intermediates and products. The observed solubilities of **1** and **2** are up to 1.0 mg ml⁻¹, and the solubility of **3** exceeds 20 mg ml⁻¹. Synthesis details on each of compounds **1**, **2**, **3**, OEG-AA and the FRET donor- and quencher-labelled AAs and their intermediates are provided in Supplementary Section 1.

Shear alignment to form macroscopic AA threads. A 2.0 wt% aqueous solution of 3 was bath sonicated for 24 h, rested for 12 h, annealed in a heating block at 80 °C for 10 h and then slowly cooled to room temperature. This solution was extruded into a bath of 40 mM sodium sulfate (Na₂SO₄) or 40 mM disodium methanedisulfonate (Na₂CH₂S₂O₆) to produce one-dimensional gels, which were pulled out of the solution and dried under ambient conditions to form the final macroscopic AA threads.

ATR-FTIR spectroscopy. ATR-FTIR spectra of aqueous samples of compound 3 dissolved at a 20 mg ml $^{-1}$ concentration in deuterated water (D $_2$ O) were acquired using an ATR-FTIR spectroscope (Bruker ALPHA II) at room temperature with a diamond crystal. Three different solvent ratios were used (D $_2$ O/DMSO = 50:50, 75:25 and 100:0), and spectra were captured upon mixing sample into the solvent as well as with 10 min, 1 h and 24 h of bath sonication after mixing (Supplementary Figs. 19 and 20). Solvent background with the same sonication time was subtracted from each spectra, and the spectra were normalized to the amide I stretching peak at 1,672 cm $^{-1}$. D $_2$ O was selected in place of water to provide less interference in the infrared region of interest.

Powder FTIR spectra (Supplementary Fig. 19) were acquired on a Thermo Fisher Scientific Nicolet 6700. Potassium bromide pellets were prepared by mixing 0.1 mg of lyophilized sample with 0.5 g of KBr (Fisher Scientific, FTIR grade). The ambient background of carbon-dioxide-free air was subtracted from each spectra.

TEM. TEM images were captured on an FEI Tecnai G2 Spirit TWIN microscope at an accelerating voltage of $120\,kV$. Grids were prepared by depositing $10\,\mu l$ of a 1 mg ml $^{-1}$ amphiphile solution onto a continuous carbon grid (Electron Microscopy Sciences, 200 mesh, copper) for 20 s, blotting to remove the solution, depositing $10\,\mu l$ of a 0.1% phosphotungstic acid solution onto the grid (Electron Microscopy Sciences) and blotting to remove the stain. TEM images of 1, 2 and 3 are shown in Supplementary Fig. 21.

X-ray scattering. SAXS samples were prepared by dissolving lyophilized powders of 1, 2 and 3 in deionized water above the solubility limit. To avoid artefacts associated with nanostructure aggregation, each sample was centrifuged at 3,000 r.p.m. and its supernatant was loaded into 2-mm-diameter quartz capillary tubes (Hampton Research). Variable temperature SAXS profiles (Supplementary Figure 26) were performed on compounds 1 and 2 in water at 1 mg ml⁻¹, and on 3 at 20 mg ml⁻¹.

Solution SAXS measurements (Fig. 2a and Supplementary Figure 26) and WAXS measurements on nanoribbon threads (Supplementary Figure 27) were performed at Beamline 12-ID-B of the Advanced Photon Source at Argonne National Laboratory with an X-ray radiation energy of 13.3 keV. DECTRIS PILATUS 300 K and PILATUS 2 M detectors were used for SAXS and WAXS, respectively. The two-dimensional X-ray scattering patterns were background subtracted to remove the water and capillary background, and processed using beamline software for reduction to one-dimensional data curves. The higher resolution of the compound 3 SAXS profile relative to those of compounds 1 and 2 is due to the notably higher solubility of compound 3.

WAXS and SAXS measurements on dried macroscopic AA threads presented in Fig. 5 were performed in vacuum on a SAXSLAB instrument using a Rigaku 002 microfocus X-ray source (CuK α radiation, 1.5418 Å) and a DECTRIS PILATUS 300 K detector. WAXS and SAXS profiles were measured at a sample-to-detector distance of 109 mm and 459 mm, respectively. Descriptions of fitting for all X-ray scattering experiments are in Supplementary Section 3c.

Cryo-TEM. Cryo-TEM grids were prepared with an FEI Vitrobot Mark IV. Holey carbon grids (Ted Pella, 300 mesh, copper) were glow-discharged, before a 3.0 μ l drop of a 2.0 mg ml $^{-1}$ amphiphile solution was pipetted onto the grids in a chamber with 100% humidity. The grids were blotted for 4 s and then plunged into liquid C_2H_6 followed by transferring to liquid N_2 . Images were captured in an FEI Tecnai Arctica microscope at an accelerating voltage of 200 kV. The defocus in data collection ranged from -1.5 to $-3.5~\mu m$.

Observation of nanoribbon length by AFM. Compound 3 solution (2.0 wt%) was prepared for AFM by following the sonication and heat treatment for making

nanoribbon thread solutions prior to their shear alignment: bath sonication for 24 h, resting for 12 h, annealing in a heating block at 80 °C for 10 h and then slow cooling to room temperature. The solution was then diluted to 0.01 wt% and a 100 μ l droplet of this diluted solution was deposited onto a cleaned mica substrate and analysed by AFM. The mica substrate was prepared through plane cleavage and cleaning with deionized H_2O . After 3 h of incubating the amphiphile solution on the clean mica, the solution was removed and then used directly for AFM imaging. Nanoribbons were imaged in tapping mode in air using a Cypher (Asylum Research, Oxford Instruments) atomic force microscope. We used AC160TS-R3 cantilevers from Olympus (nominal spring constant 26 N m $^{-1}$ and resonance frequency of 300 kHz in air). AFM images were recorded at 512 pixels \times 512 pixels at a scanning speed of 0.65 Hz.

SEM. SEM images were recorded on a Zeiss MERLIN field emission microscope operating at a $1-3\,\mathrm{kV}$ accelerating voltage to resolve the higher-order structure of the dried AA nanoribbon threads. A secondary electron detector set to $120-200\,\mathrm{pA}$ was used for imaging. The SEM micrograph in Supplementary Fig. 29 was coated with $10\,\mathrm{nm}$ Au by sputtering on a MS Q150T ES coater.

FRET. A fluorescent donor (EDANS) and quencher (DABCYL) were each covalently tethered to the head group region of an AA (Supplementary Fig. 31). AAs were prepared at concentrations of 0.1 to 0.5 mM in water and co-assembled with 5 mol% donor- or quencher-tagged analogues. Fluorescence intensities were measured on a Varian Cary Eclipse spectrophotometer operating at an excitation wavelength of 334 nm with excitation and emission slits set at 5 nm. A fluorimeter scan rate of 600 nm min⁻¹ was used, and the photomultiplier tube detector voltage was 600 V. A further description of the FRET study and control experiments is provided in Supplementary Section 3f.

Stiffness determination by topographical analysis of nanoribbon contours. Compound 3 nanoribbons were imaged in tapping mode in water using a Bruker/JPK Nanowizard 4 atomic force microscope using BL-AC40-TS cantilevers from Olympus (nominal spring constant $0.1\,\mathrm{N\,m^{-1}}$ and resonance frequency of ~25 kHz in water). AFM images were recorded at 512 pixels x 512 pixels at a scanning speed of 10 Hz. Fluctuations of ribbon shapes from AFM images were statistically processed using the Easyworm software tool⁴³, which traces parametric splines to the contours of many ribbons of the same sample (in this experiment, n=29 ribbons). The persistence length P extracted from this data is used to calculate each nanoribbon's flexural rigidity by scaling to thermal energy, and the Young's modulus E is ultimately evaluated by dividing the flexural rigidity by the area moment of inertia for the nanoribbon. A detailed description of sample preparation and experimental details is provided in Supplementary Section 3g.

Yield strength determination by sonication-induced scission. We measure the yield (tensile) strength σ^* by a sonication-induced fibril scission technique, as detailed in our previous work. In short, sonication creates collapsing cavitation bubbles, causing fluid velocity fields to trap fibrils and exert shear forces on them. This leads to fibril extension in opposite directions and mechanically induced rupture at the site of highest stress. After prolonged sonication time, fibril length distribution reaches a plateau and the size of fragments that belong to a sample fall in a 'terminal range' correlated to the yield strength of the nanoribbons.

A Qsonica Q500 sonicator with a 2-mm-diameter microtip was used to sonicate 10 ml of a $0.5\,\mathrm{mg\,ml^{-1}}$ aqueous solution of compound 3 nanoribbons. A vibrational frequency of $20\,\mathrm{kHz}$ and amplitude of 25% were used during the experiment, which lasted for 2 h of 'sonication on' time with a 5-seconds-on/3-seconds-off pulse. Sonicating power was held at 30 W cm $^{-2}$ to ensure cavitation. The solution was held in an ice bath for the duration of the experiment to prevent solvent evaporation and tip breakage during sonication. Images of fragments after sonication were captured by TEM and AFM. A comprehensive discussion on this experimental technique is provided in Supplementary Section 3h.

Polarized light microscopy. The liquid crystalline state of gelled AA nanoribbons was observed using an Olympus BH-2 microscope equipped for polarized light imaging. Gelled nanoribbons were analysed immediately after extrusion onto a cleaned glass microscope slide while still wet. Images were captured with a Pixelink PL-E535CU camera.

Tensile testing of macroscopic AA threads. Macroscopic mechanical properties of compound 3 AA threads were characterized using a uniaxial bench-top tester (CellScale UStretch) equipped with a 0.5 N load cell. Threads were prepared following the shear alignment procedure described previously, then fixed with epoxy glue on two tailored cardboard supports gripped to the standard spring-loaded clamps of the testing machine. The glue was allowed to set for 24h. Threads with counterions of either sulfate (n=6) or methanedisulfonate (n=6) were tested at a constant stretch velocity of 25 μm s⁻¹. Each thread was imaged with an optical microscope to determine its mean diameter from multiple cross-sections, which varied between 55 μm and 80 μm for all threads.

Raw data from the UStretch software was exported and analysed separetly in MATLAB. Force measurements were converted to stress using the initial cross-sectional area. Displacement of the moving end (u_t) was converted into engineering strain using the initial length of each thread (L_0) as u_t/L_0 . The Young's modulus was extracted by fitting each experiment to a linear elastic constitutive equation using a nonlinear least-squares algorithm. The extensibility (maximum strain at failure) was extracted directly from the stress–strain curves at the maximum stress before breakage. Values are reported as average \pm one standard deviation.

Data availability

The data generated and analysed during this study are available from the corresponding author on reasonable request.

Acknowledgements

We thank E. Deiss-Yehiely and C. Settens for their helpful input. We thank R. Allen and L. Hopkins for contributing graphics shown in the figures. We acknowledge J. Tian and S. Kallakuri for contributions to synthesis of early stage AAs that led to the molecular designs incorporated in this report. This material is based upon work supported by the National Science Foundation under grant no. CHE-1945500. This work was supported in part by the Professor Amar G. Bose Research Grant Program, the Abdul Latif Jameel Water and Food Systems Lab, and the MIT Center for Environmental Health Sciences under NIH Center grant P30-ES002109. D.-Y.K. acknowledges the support of the National Research Foundation of Korea's Basic Science Research Program and Chonbuk National University Fellowship Program. T.C.-T. and W.R.L. acknowledge the support of the National Science Foundation Graduate Research Fellowship Program under grant no. 1122374. T.C.-T. acknowledges the support of the Martin Family Society of Fellows for Sustainability. G.L. acknowledges support from the Université d'Evry-Paris Saclay. This work made use of the MRSEC Shared Experimental Facilities at MIT supported by the National Science Foundation under award number DMR-14-19807 and the MIT Department of Chemistry Instrumentation Facility. X-ray scattering measurements were performed at beamline 12-ID-B of the Advanced Photon Source, a US Department of Energy Office of Science User Facility operated for the US Department of Energy Office of Science by Argonne National Laboratory under contract no. DE-AC02-06CH11357.

This work was performed in part at the Harvard University Center for Nanoscale Systems cryo-TEM facility, a member of the National Nanotechnology Coordinated Infrastructure Network, which is supported by the National Science Foundation under award no. 1541959.

Author contributions

T.C.-T., D.-Y. K. and J.H.O. conceived and designed the experiments. D.-Y.K. and T.C.-T. synthesized materials with assistance from W.R.L. and A.J.L.; T.C.-T. and D.-Y.K. performed chemical characterization of all samples. T.C.-T. performed conventional TEM and cryo-TEM. Y.C. and T.C.-T. performed SEM. G.L. performed AFM and statistical topographical analyses. G.L. performed sonication-induced scission measurements, imaging with AFM and TEM, and analysis of data. A.J.L. performed FRET measurements and analysis of the data. X.Z., T.C.-T. and Y.C. performed solution X-ray scattering and analysis of the data. A.J.L. and Y.C. conceptualized nanoribbon thread processing, and Y.C. and M.G. prepared nanoribbon threads. M.G. performed tensile testing of nanoribbon threads and analysis of the data. T.C.-T. and Y.C. performed X-ray scattering of solid-state nanoribbon threads and analysis of the data. J.H.O., T.C.-T and Y.C. cowrote the manuscript. J.H.O. provided project administration, funding acquisition and supervision. All authors discussed the results and commented on the manuscript.

Competing interests

The authors declare no competing interests.

Additional information

Supplementary information is available for this paper at https://doi.org/10.1038/s41565-020-00840-w.

Correspondence and requests for materials should be addressed to J.H.O.

Peer review information *Nature Nanotechnology* thanks the anonymous reviewers for their contribution to the peer review of this work.

Reprints and permissions information is available at www.nature.com/reprints.